CHEMISTRY OF MATERIALS

ARTICLE

pubs.acs.org/cm

Toward a Reliable Synthesis of Strontium Ruthenate: Parameter Control and Property Investigation of Submicrometer-Sized Structures

Amanda L. Tiano,[†] Alexander C. Santulli,[†] Christopher Koenigsmann,[†] Mikhail Feygenson,[‡] M.C. Aronson,[‡,§] Richard Harrington,[†,∥] John B. Parise,[†,∥] and Stanislaus S. Wong*[,†,‡]

[†]Department of Chemistry, State University of New York at Stony Brook, Stony Brook, New York 11794-3400, United States

[‡]Condensed Matter Physics and Materials Science Department, Brookhaven National Laboratory, Upton, New York 11973, United States

[§]Department of Physics and Astronomy, State University of New York at Stony Brook, Stony Brook, New York 11794-3800, United States

[∥]Department of Geosciences, State University of New York at Stony Brook, Stony Brook, New York 11794-2100, United States

Supporting Information

ABSTRACT: $SrRuO_3$ (SRO) has been studied extensively at the bulk and thin film scales for a variety of applications, such as multilayer devices, field-effect devices, multiferroics, and even ferroelectric random access memory (FeRAM). Conversely, the exploration of SRO nanoscale and submicrometer scale structures in terms of both synthesis and applications has been significantly limited. Herein, we are the first to report on the synthesis of SRO submicrometer-sized particles via a molten-salt method. We have accomplished this by systematically probing experimental parameters such as precursors, type of salt, annealing time, annealing temperature, surfactant, cooling rate, and reaction atmosphere in an effort to predictably control the resulting size, shape, and morphology of the SRO product particles. In particular, by quenching the reaction at a cooling rate of 100 °C/min, we can produce rounded SRO particles averaging 149 ± 100 nm in size. Moreover, with the addition of a mixture of mineral oil in Triton X-100, the final SRO particles are highly faceted, single-crystalline octahedra, averaging 126 ± 45 nm in size. Apart from the choice of molten salt which primarily controls chemical composition of SRO, we have determined the most important experimental parameter for shape and aggregation control is the surfactant, because of a combination of its hydrophobic and hydrophilic characteristics. We have found that the decomposition of the surfactant promotes the formation of $SrCO_3$, which is consistent with the generation of SRO through the reaction of $SrCO_3$ with RuO_2. Our successful syntheses have allowed us to explore physical properties, that is, magnetic and electronic, of these submicrometer-sized SRO particles, which are in good agreement with bulk SRO. Furthermore, we have also explored the potential of our as-synthesized particles as effective methanol oxidation reaction (MOR) catalysts for direct methanol fuel cells (DMFCs). Not only are our as-synthesized SRO particles MOR active but also our well-defined faceted octahedra exhibit a 4-fold increase in mass-activity and a 4-fold increase in surface area by comparison with the rounded particles, thereby emphasizing a clear advantage of faceted submicrometer SRO for electrochemical applications.

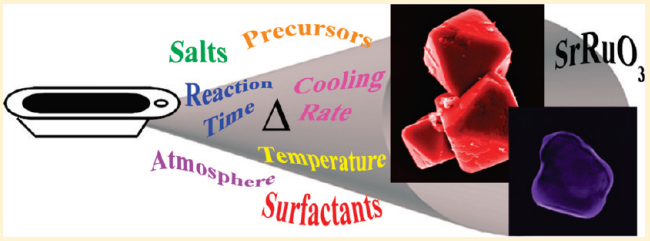

KEYWORDS: strontium ruthenate, molten salt synthesis, methanol oxidation reaction, catalysis, perovskite

1. INTRODUCTION

Transition metal oxides, specifically those possessing perovskite-type structures, have been the focus of many experimental and theoretical studies, because of the interesting properties that these materials possess, rendering them as desirable candidates for practical applications such as nanoscale electronics, drug delivery, biological probes for diagnosis and detection, sensors, solar cells, fuels cells, and catalysts. Of particular interest are the ternary ruthenates, $ARuO_3$, because of their attractive transport and magnetic properties.[1] Of this family of materials, strontium ruthenate, $SrRuO_3$, has prompted a considerable degree of interest, which can be attributed to its plethora of exceptional properties. Specifically, $SrRuO_3$ (SRO) is highly conductive[2] up to the Curie temperature, $T_C = 160$ K, and is a rare 4d ferromagnetic material[3] with a magnetic moment of 1.1 μ_B[4,5] with reported values ranging from 0.9−1.6 μ_B.[5] Moreover, strontium ruthenate is chemically stable with excellent thermal properties,[6] which have been demonstrated for both bulk and thin films. In particular, for bulk SRO, its chemical stability in both oxidizing and inert atmospheres persists up to 1200 K, while a reducing atmosphere easily induces decomposition into SrO and Ru metal at 800 K,[7] analogous to experiments conducted on epitaxial thin films of SRO, which have revealed that an adequate amount of oxygen was crucial for stability up to 720 °C.[6]

The structure of $SrRuO_3$ consists of corner-shared RuO_6 octahedra with strontium atoms in the interstices and, interestingly,

Received: October 13, 2010
Revised: June 6, 2011
Published: June 28, 2011

exhibits crystal structure transformations with variations in temperature. At low temperatures, below 820 K, SRO exists as a distorted orthorhombic structure (*Pbnm*), followed by conversion to a tetragonal structure ($I4/mcm$) between 820 and 950 K. Above 950 K, it is the cubic ($Pm\bar{3}m$) structure, as expected for a perovskite material.[8] In addition to the aforementioned structural properties, thin films of SRO have been shown to exhibit a metal-to-insulator transition (MIT) which has been observed at four monolayers of thickness.[9] Furthermore, $SrRuO_3$ possesses a sizable magnetoresistance,[10] and also displays an anomalous Hall effect.[11,12] Several theoretical[8,13−17] and experimental studies, involving spectroscopic, optical, and transport techniques,[9,11,18−27] have been conducted to probe the source of these interesting properties. These investigations have suggested that the ruthenium 4d orbitals and subtle structural changes, such as Ru−O−Ru distances and angles,[28,29] greatly influence the observed magnetic, transport, and thermodynamic properties of SRO.

Because of these appealing properties as well as the close lattice match to ferroelectric oxides and superconductors, strontium ruthenate has been investigated for applications in multilayer devices,[30−33] field-effect transistors,[34,35] conductive materials, as well as in multiferroics.[36] Another useful application of $SrRuO_3$ has been its potential, either as a bottom electrode or as buffer layers in ferroelectric random access memory (FeRAM),[37,38] which has high resistance to degradation and maintains the ability to retain information even with a loss of power.[39] With respect to their multitude of electronic and magnetic properties, SRO has recently been highlighted as a potential anode catalyst in direct methanol fuel cells (DMFCs),[40,41] an application driven by the gainful search for inexpensive and stable replacements for precious metal catalysts. There has been a significant amount of interest in the development of acid-fast metal oxide nanostructures, which can act as both high surface area supports and co-catalysts in the presence of transition metal catalysts.[42] Though there have been only a few reports wherein metal oxides have been used directly as stand-alone catalysts,[43−45] SRO has demonstrated significant potential as an effective MOR catalyst in a high throughput study of a variety of metal oxides analyzed under simulated DMFC conditions.[46,47]

As demonstrated by our group, the synthesis of nanoscale and submicrometer-sized perovskite and pseudoperovskite materials has been accomplished in the past,[48−52] and the investigation of their size-dependent properties[53−55] has proven to be advantageous in the trend toward device minimization. To the best of our knowledge, the synthesis and exploration of SRO has been significantly limited to that of thin films[6,9,22,24,34,38,56−60] and nanoscale patterned thin films[61] produced via various deposition and sputtering techniques. Only Pagnaer and co-workers[62] and Mercurio et al.[63] have reported the synthesis of SRO powders via sol−gel methods. However, neither group provided any definitive visual confirmation of the resultant particle size and morphology of this material. More recently, another group demonstrated the synthesis of nanostructured SRO by citrate-nitrate and coprecipitation methods as catalysts for a hydrogen evolution reaction.[64] However, electron microscopy images revealed that the dimensions of as-synthesized particles were closer to the micrometer size than to the nanoscale and, in addition, the XRD patterns revealed the presence of large impurities which may have affected their catalytic performance.

The novelty of our protocol can be described in a 3-fold approach. First, to the best of our knowledge, we are the first to report the successful synthesis of nearly pure SRO submicrometer particles with only minor impurities achieved via a molten salt synthesis (MSS). Second, we have systematically probed the effects of various experimental parameters to achieve the optimal reaction conditions for the formation of SRO particles. Specifically, we have explored the individual roles of the nature of the salt medium, precursors, surfactants, ratios of starting materials, annealing temperatures, annealing times, cooling rates, and atmospheric conditions upon SRO nanoparticle synthesis. More importantly, the systematic variation of these parameters has allowed us to correlate their individual effects with the resulting reaction products and, as such, we have gained a practical understanding of how to tailor and predictably control the chemical composition, size, and morphology of the resultant particles. Lastly, our successful synthesis has allowed us to innovatively explore the physical properties of these SRO particles by comparison with their bulk and thin film counterparts, and, more importantly, probe their electrocatalytic properties for the MOR process as a function of particle morphology and size.

2. EXPERIMENTAL SECTION

All chemicals were used as purchased, without any further purification. In the optimized synthesis, $Sr(OH)_2 \cdot 8H_2O$, RuO_2 nanoparticles, NaCl/KCl, and 1% mineral oil in Triton X-100 surfactant were ground up together using a mortar and pestle in a molar ratio of 1:1:20:3. Pure, spherical RuO_2 nanoparticles, averaging 20 nm in diameter, were synthesized using an existing sol−gel procedure,[65] and subsequently purified with H_2O_2 to oxidize any residual ruthenium metal. The reaction mixture was transferred to a porcelain crucible, placed in a quartz tube furnace, heated to 700 °C at a heating rate of 5 °C/min, and rapidly quenched at a cooling rate of 100 °C/min upon removal from the furnace, with all heating steps conducted under a continuous flow of air. After subsequent cooling to room temperature, the black-colored product was washed twice with aliquots of distilled water, isolated with centrifugation and decantation, and then placed in a drying oven at 80 °C. To remove any $SrCO_3$ impurities present, samples were washed with 0.1 M HCl (Supporting Information, Figure S1). As previously mentioned, experimental parameters were systematically varied to determine the optimal conditions. Specific experimental details for each reaction performed (manifested as samples A through XX), including materials, suppliers, and methods used, are provided in the Supporting Information section in Table S1. In addition, the sample preparation and techniques for characterization have also been provided in the Supporting Information section.

3. RESULTS AND DISCUSSION

Of the many types of reaction parameters investigated, we found that the nature of the salt, choice of surfactant, reaction atmosphere, and annealing time/cooling rate are the most critical parameters for effectively tailoring the composition, size, and morphology of the resultant particles. By systematic variation of the remaining parameters, that is, annealing temperature, nature of precursors, and ratio of reagents, we found that they did not contribute to a dramatic improvement in the resultant product (see Supporting Information, Table S1). All of these are discussed in detail in the Supporting Information section. Herein, we discuss the real and tangible effects of the most important parameters and their individual role in reliably tailoring the synthesis toward submicrometer $SrRuO_3$.

3.1. Effect of Salt on Product Composition and Morphology. One of the critical parameters involved in a molten salt synthesis is the choice of the molten salt itself because of the complementary

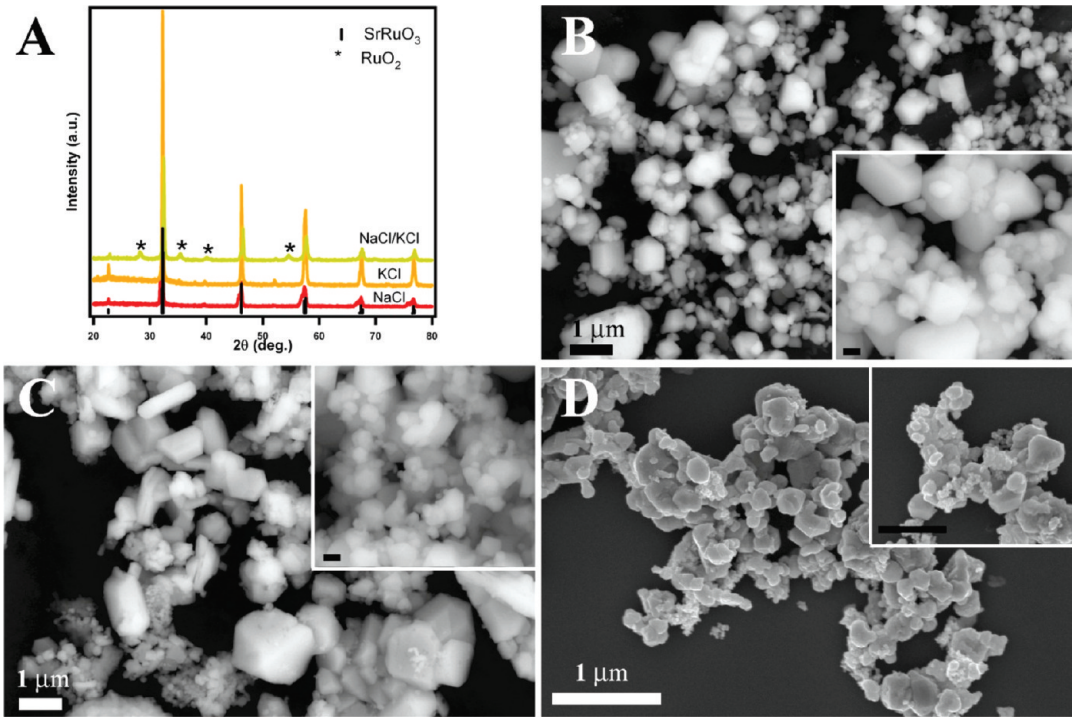

Figure 1. XRD analysis of samples (A) prepared using KCl, NaCl, and NaCl/KCl as molten salts compared to JCPDS standards for RuO_2 (#73-1469) and $SrRuO_3$ (#82-2156), shown along with corresponding SEM images (B), (C), and (D), respectively. Scale bars in the insets of (B) and (C) correspond to 200 nm. Inset scale bar in (D) is 500 nm.

and necessary roles the salt can fulfill in the reaction. First, the molten salt solution not only dictates the reaction temperature based on its melting point but also, in many cases, such as the chlorides, acts as a high-temperature solvent for the reaction. In addition, some molten salt solutions can directly participate in the reaction, either through a catalytic role or by consuming reactants. Most importantly, the solubilities of the individual precursor materials within the molten salt solution are crucial for the desired reaction to occur.[52] Thus, it is clear that the nature of the salt should be carefully chosen based upon all of these criteria.

As such, we prepared numerous samples by employing a wide variety of molten salts at reaction temperatures above their respective melting points (see Supporting Information for melting points and eutectic ratios) to determine the best salt with respect to composition and particle morphology (samples A−K). By this process, we deduced that many salts and eutectics, namely, $NaNO_3$, LiCl, NaF/KF, NaOH/KOH, $SrCl_2 \cdot 6H_2O$, Na_2SO_4, and $NaNO_3$/NaOH, were poor reaction media. We make this observation either because of (a) their inability to produce pure $SrRuO_3$ entirely or (b) because the resulting product composition was dominated by impurities (Supporting Information, Figure S2). Of all the salts investigated, NaCl, KCl, and the NaCl/KCl eutectic demonstrated the most promise for fabricating strontium ruthenate, an observation which could likely be attributed to higher precursor solubility and mobility within these molten fluxes. Specifically, these three molten salts evinced an ease of producing the desired composition (Figure 1A) with differing morphological outcomes. By SEM analysis, the morphologies of samples synthesized using KCl and NaCl as stand-alone molten salts yielded the presence of particles (Figure 1B, 1C) without a defined morphology, though there was some faceting observed on the particle surfaces themselves. In addition, some disk-shaped particles were noted via SEM analysis of SRO samples derived from both the NaCl and KCl molten salt media. By contrast with the individual molten salts, utilizing a common eutectic NaCl/KCl as the solvent (Figure 1D) did not yield any disk-shaped particles, though a degree of faceting of some of the particles was still achieved. These particular results emphasize the importance of using a chloride-based salt for synthesizing $SrRuO_3$ and, moreover, this is consistent with observations in the literature, which demonstrate that the choice of anion is likely an important synthetic variable to consider in a molten salt synthesis.[66,67]

These favorable observations, namely the presence of only a single morphology coupled with strong evidence for generating the desired chemical composition within this sample, led us to deduce that the NaCl/KCl molten salt represented the optimal choice of reaction medium. Hence, with the fixed selection of our salt, we continued to systematically exploit variations in other experimental parameters with the aim of generating a monodisperse $SrRuO_3$ sample.

3.2. Effect of Surfactant on Particle Morphology. Inspired by the observation of some faceting of the particle surfaces, we aimed to next focus on the addition of surfactants to enhance the faceting of the as-synthesized particles. Often, the use of a surfactant within the context of a molten salt synthesis is advantageous for exhibiting control over the morphology of the product; this observation has been presented in the literature for a wide variety of nanomaterials.[68−73] Moreover, as a majority of surfactants are liquids, their inclusion during the grinding process can assist in coating the precursor materials. Many solid surfactants have low melting points, and will liquefy well below decomposition, thereby aiding in reactant dispersion. Additionally, surfactants can assist in reducing impurities on the surfaces, and most importantly, preventing undesirable aggregation.[74−76]

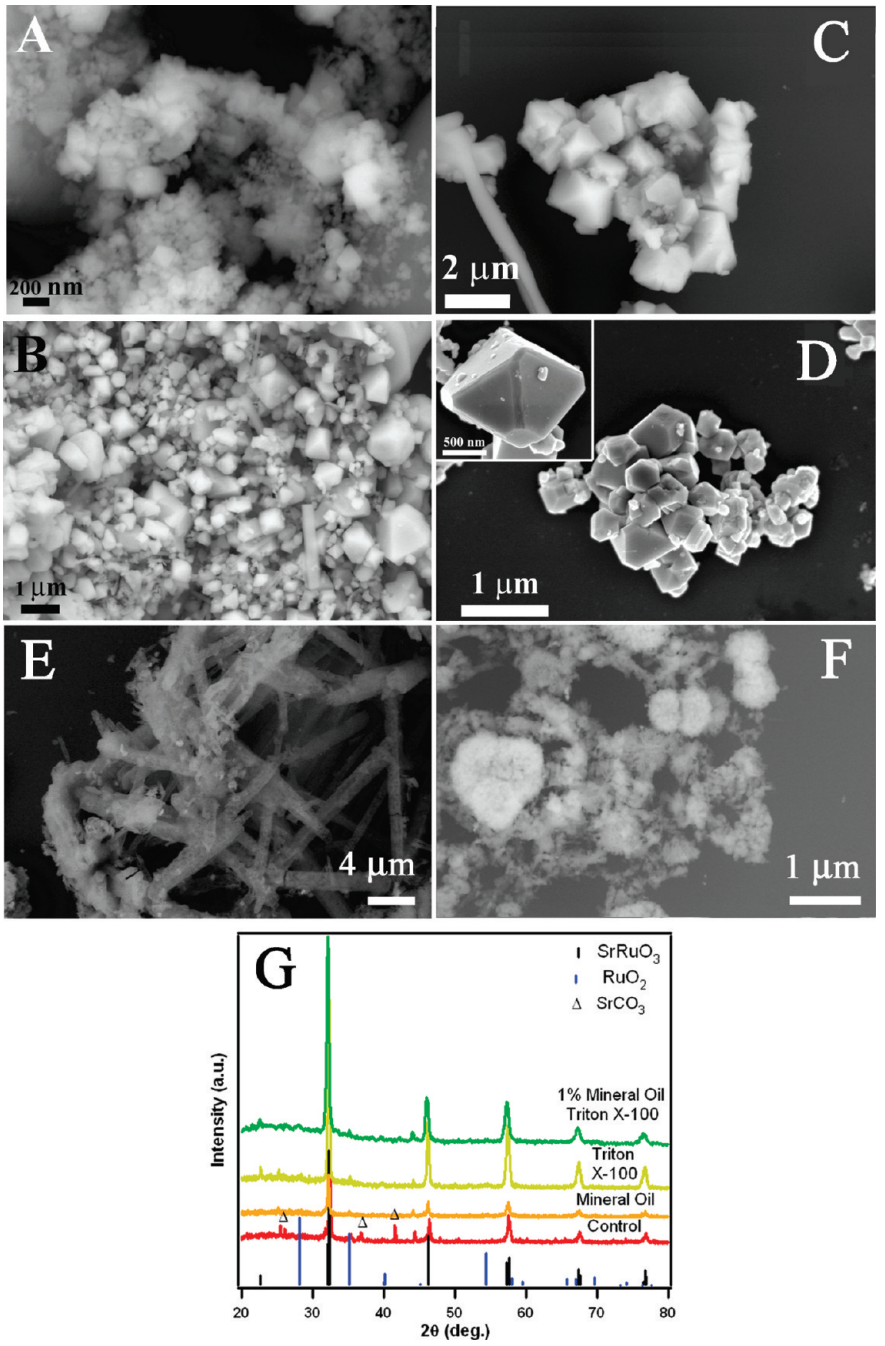

Figure 2. SEM images for as-prepared SRO samples, comparing the effects of surfactants upon the resultant particle morphology. Samples correspond to the presence of no surfactant (A) and Triton X-100 (B), mineral oil (C), 1% mineral oil in Triton X-100 (D), the absence of surfactant at 400 °C (E), and 1% mineral oil in Triton X-100 at 400 °C (F). Corresponding XRD patterns (G) for the samples shown have been compared with the JCPDS standard for $SrRuO_3$ (#82-2156) and RuO_2 (#73-1469).

Hence, our next goal was to test and analyze the presence of various surfactants within the reaction mixture to determine what effect, if any, each of these had on the resulting morphology of as-synthesized SRO particles. The surfactants employed in this study included Igepal CO-520 (NP5), Igepal CO-620 (NP9), 4-(1, 1, 3, 3-tetramethylbutyl) phenyl-polyethylene glycol (Triton X-100), cetyltrimethylammonium bromide (CTAB), octadecylamine (ODA), sodium dodecylsulfate (SDS), as well as polyvinylpyrrolidone (PVP) with M_w values of 30 000 and 1 300 000, oleic acid, mineral oil, decane, and ethylene glycol (samples M−Y). A surfactant-free control experiment (sample L) was also performed to observe potential differences in the morphology and size of the final products. The product from the control experiment (Figure 2A) consisted of rounded, polydisperse SRO particles (90%) in addition to SRO octahedra/cubes (10%) with some minor $SrCO_3$ impurities, as evidenced by the XRD results shown in Figure 2G.

Of all the surfactants investigated, only the samples produced with Triton X-100 and mineral oil exhibited a significant degree of control over the growth of as-synthesized particles. Specifically,

dx.doi.org/10.1021/cm1029497 |*Chem. Mater.* 2011, 23, 3277–3288

SEM analysis showed that the sample prepared with Triton X-100 (Figure 2B) yielded octahedra and cubes (334 ± 135 nm) as the dominant morphology with a few polydisperse particles present. Though XRD data evinced a minor $SrCO_3$ impurity (Figure 2G), we have demonstrated herein that this can be easily removed using an HCl acid wash (Supporting Information, Figure S1). Hence, even with the large particle size distribution presented, this sample showed the greatest promise in terms of exhibiting effective control over the final product shape. The SRO sample produced with mineral oil evinced a similar morphology by SEM (Figure 2C); the particles (789 ± 253 nm) were highly faceted octahedra but were also substantially aggregated and possibly annealed together. An additional sample produced using a mixture of the two components (1% mineral oil in Triton X-100) produced highly faceted particles (Figure 2D), which were larger in size than what was isolated from the pure Triton X-100 sample (e.g., 577 ± 282 nm) and included a large quantity of octahedra present (Figure 2D inset). Based upon these results, it could be reasonably hypothesized that whereas the hydrophobic groups in the Triton X-100 surfactant may be responsible for the faceting observed, some degree of surfactant hydrophilicity may be necessary to prevent aggregation. This is apparent from the highly aggregated product synthesized using the pure hydrophobic mineral oil alone. Hence, it is evident from these results that both shape and aggregation control can be achieved with these systems.

Since most surfactants are organic in composition, the material is likely either oxidized or decomposed completely at ~400 °C. This fact leads to the following question: What is the true influence of the surfactant upon the morphology of the particles in a molten salt synthesis? With solution-based methods for synthesizing submicrometer-sized as well as nanoscale materials, surfactants are known either to form micelles in solution or adsorb onto particular facets and alter their growth rates. However, the exact mechanism by which surfactants can induce shape selectivity under molten salt conditions is still undetermined, as many molten salt reactions occur at temperatures well above the boiling points of most surfactants. Under these high temperature conditions, it is unlikely that any surfactant remains in the molten flux, so one could easily conclude that the surfactant cannot have a direct effect upon the particle morphology. Still, a preponderance of examples in the literature clearly demonstrates that the inclusion of surfactants in molten salt syntheses leads to excellent morphological control,[74,75,77,78] which directly mirrors the effects both we and others have observed with solution-based techniques. Hence, the incorporation of surfactants plays a key role in shape control during molten salt reactions despite the fact that no definitive mechanism has been proposed previously.

Herein, to gain mechanistic insight, we have attempted to investigate the specific role of the surfactants in this synthetic protocol to shed some new light onto this unexplored area of molten salt synthesis. A previous investigation of the decomposition of Triton X-100 in air revealed that the hydrophilic end of the surfactant decomposes to carbonates first.[79] It has been demonstrated that the formation of carbonates can aid in reducing the melting temperature of the eutectic.[74,75,80] As a reference, a KCl-NaCl-Na_2CO_3 eutectic mixture in a nearly 1:1:1 ratio has a melting point of 573 °C,[81] which is significantly lower than the NaCl-KCl melting point of 657 °C, an observation which could aid in accelerating the production of $SrRuO_3$ in the latter case. Furthermore, below 350 °C, the oxidation of Triton X-100 is restricted to its hydrophilic groups, while its hydrophobic group persists at a much slower rate of decomposition. Thus, it would seem likely that the hydrophobic groups would be participating in the traditional surfactant role of dispersal, consistent with the SEM results in Figure 2, whereas the hydrophilic groups may contribute to the reduction of the eutectic point through the formation of carbonates. Subsequent investigation of the reaction via *in situ* thermogravimetric analysis (TGA) and differential thermal analysis (DTA) revealed that there was no measurable deviation in the melting point of the melt by inclusion of the surfactant (Figure 3). Thus, even if carbonates were being formed, their amounts either may be too low or might exist as an intermediate, which, in any event, did not noticeably alter the eutectic melting point.

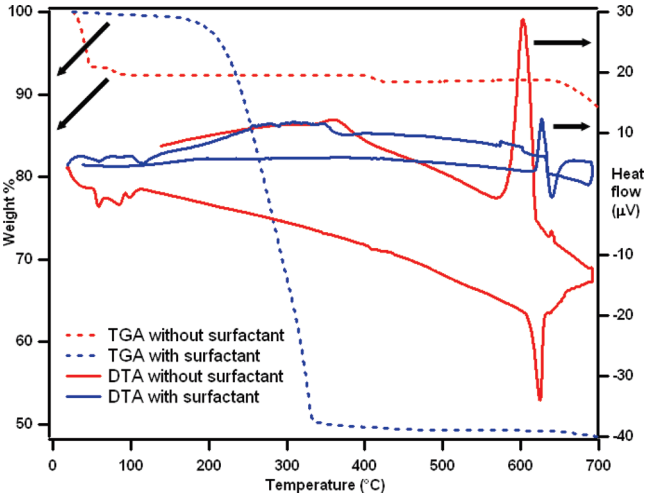

Figure 3. TGA (dashed) and DTA (solid) results for the reaction mixture either with (blue) or without (red) surfactant heated to 700 °C at a rate of 5 °C/min in air.

To investigate shape control effects, we conducted two additional reactions. One involved the use of 1% mineral oil in the presence of Triton X-100. The second was a control experiment without any surfactant. Both molten salt mixtures were heated to 400 °C, a value above the complete decomposition temperature of the surfactant but below the optimal melting temperature necessary to generate pure SRO, and subsequently quenched. The "products" were probed by SEM to determine any differences in composition and morphology upon inclusion of the surfactant to the reaction mixture. Indeed, the resulting "product" at 400 °C, specifically $SrCO_3$, was demonstrated to be drastically different in morphology for the two samples. That is, the sample prepared without any surfactant showed the presence of micrometer-sized 1-dimensional $SrCO_3$ (Figure 2E) whereas in the sample with 1% mineral oil in Triton X-100 surfactant, small spherical $SrCO_3$ particles (Figure 2F) were predominant. These significant results confirmed the shape controlling ability of incorporated surfactants, but more importantly, they demonstrated that the presence of surfactant could dictate the morphology of the intermediate species formed *in situ*. Thus, as with titania systems we have previously investigated in the group,[82] the shape and size of the reaction intermediates can have a direct impact upon the product's morphology. Specifically, shape control of the final resultant SRO product in this molten salt synthesis process was achieved by the inclusion of a surfactant species, which specifically determined the morphology of the strontium carbonate intermediate.

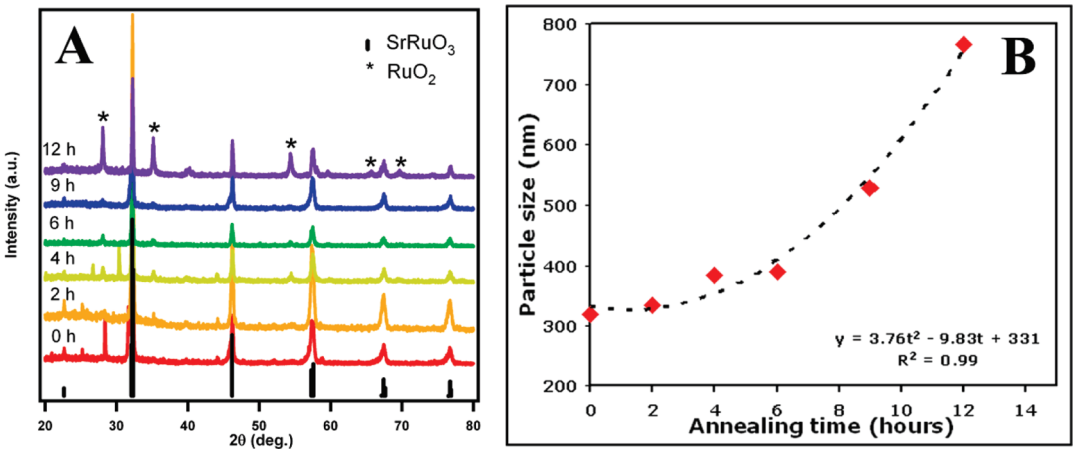

Figure 4. XRD patterns for samples annealed at 0, 2, 4, 6, 9, and 12 h (A) and the corresponding plot of the resulting particle sizes with respect to annealing times (B).

3.3. Effect of Atmosphere on Product Composition and Morphology. Often with the molten salt method, a continuous flow of air, as we have employed thus far, is used during the synthesis. However, it has been demonstrated that different gases used during synthesis can drastically alter the outcome, in particular the morphology and chemical composition of the product.[83−86] For the sake of completeness, we aimed to determine if the atmospheric conditions within the sealed tube furnace had any effect upon the production of SRO (samples N, EE−GG). As such, we employed three types of gases, namely, house air, nitrogen, and extra-dry air, all of which were passed through the quartz tube at identical flow rates and monitored with a bubbler. We define "house air" as compressed air supplied through the building infrastructure as opposed to air from a compressed gas cylinder. For comparison, we prepared a sample in which the quartz tube was sealed with no apparent gas flow. In cases where air in some formulation was employed, the samples successfully yielded SRO. Not surprisingly, for samples prepared either in an inert atmosphere (N_2) or in the absence of gas flow within the sealed tube, XRD analysis did not detect any SRO in these products. In particular, the XRD pattern for the sample prepared in N_2 showed the presence of metallic Ru, indicative of a reducing atmosphere arising from the decomposition of Triton X-100 in an inert atmosphere. This is consistent with the instability of bulk SRO in a reducing environment.[7] Conversely, as bulk SRO is stable to very high temperatures in an oxidizing atmosphere, it is likely that the presence of O_2 is necessary to produce SRO under these reaction conditions. As such, we have determined that air is the most desirable gas medium to employ for the fabrication of SRO particles.

While samples prepared in the presence of air in some form can give rise to SRO, there were noticeable differences in the size and morphology of the resulting products. Specifically, in the case of "house air", the resultant morphology consisted of octahedra and cubes, averaging 334 ± 135 nm on an edge. On the other hand, the presence of extra dry compressed air yielded particles which were significantly larger in size, for example, 574 ± 377 nm, as compared with those synthesized using only "house air". The primary inherent difference between these two gases is the water content. Specifically, water vapor, under these reaction conditions, may play a role in the formation of smaller, faceted particles.

The nature of the precise effects of water vapor upon particle formation is beyond the scope of this paper. However, it has been shown that the presence of water in molten salt media affects the resulting nanomaterials by changing the vapor pressure as well as the acidity and basicity of the flux, all of which can have an impact upon the solubilities of the precursor materials.[87] We can reasonably conclude that the presence of water enhances the solubility of the reactants within the flux, thereby promoting the desired reaction to produce SRO. Thus, it is clear from our experiments that humid "house air" is preferable to the use of extra-dry compressed air with respect to the optimized synthesis of submicrometer-sized SRO particles.

3.4. Effect of Annealing Time and Cooling Rate on Particle Size. Next, several identical samples were prepared in a series of different annealing times ranging from 0 to 12 h (samples N, Z, and AA−DD), respectively, to determine their effect, if any, upon the resultant product shape and size. The 0 h sample refers to (i) heating of the crucible up to 700 °C followed by (ii) immediate turning off of the furnace to most rapidly cool it back to ambient conditions.

In all cases, the XRD analysis (Figure 4A) reveals that the samples are mainly composed of SRO with minor impurities, typically either $SrCO_3$ or RuO_2. Subsequent analysis with SEM allowed us to investigate the progression of the reaction and evolution of the resultant particles.

Accordingly, a plot of particle size versus reaction time (Figure 4B) highlights a trend of increasing particle size with increasing annealing time, which is shown to be parabolic in nature. Based upon the overall trend of the system, we can attribute the increase of SRO particle sizes at increased annealing times to the Ostwald ripening phenomenon,[88] which is consistent with observations in the literature.[70,75] Thus, if smaller particles are desired, reaction times between 0 and 2 h would be preferable to produce optimal products.

Additionally, we investigated the effect of the cooling rate upon the resultant particle size. In all of the syntheses thus far, we employed a slow cooling rate of ∼3.5 °C/min (sample N). Under effectively identical conditions, by contrast, when the reaction is quenched at a fast cooling rate of ∼100 °C/min, the product consists of malformed SRO (Supporting Information, Figure S3A) particles (sample SS) which, on average, are significantly smaller in size, measuring only 149 ± 100 nm (Supporting Information,

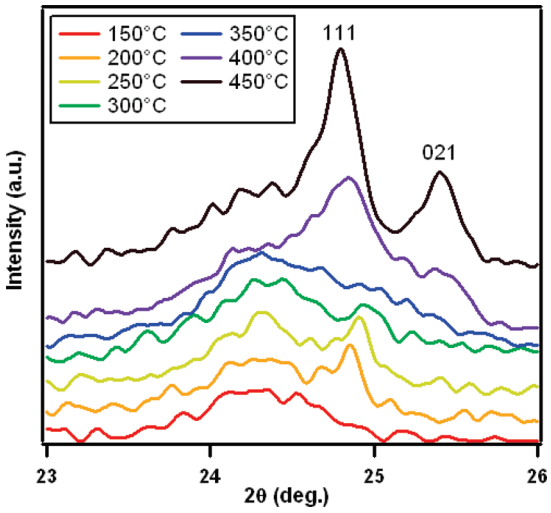

Figure 5. Temperature-dependent XRD patterns of the mixture from 150 to 450 °C, showing the formation of $SrCO_3$ by observation of the 111 and 021 peaks.

Figure S3B). From these two simple experiments, we can reasonably conclude that a longer cooling time allows for the reaction to continue upon cooling until the temperature is low enough to naturally quench the reaction, thereby resulting in a more complete faceting of the particles. On the other hand, manually quenching the reaction with fast and rapid cooling quickly halts the reaction. Hence, only smooth, nondescript particles are observed by SEM analysis, since insufficient time was provided for to allow for the particles to properly ripen and form facets.

3.5. Investigation of the Reaction Mechanism. In addition to individual reaction parameters, we aimed to consider the possible chemical reactions which would be responsible for the production of SRO within the flux. Accordingly, we propose three potentially plausible reactions below.

$$SrO + RuO_2 \rightarrow SrRuO_3 \quad (1)$$

$$SrCO_3 + RuO_2 \rightarrow SrRuO_3 + CO_{2(g)} \quad (2)$$

$$Sr + RuO_2 + \frac{1}{2}O_2 \rightarrow SrRuO_3 \quad (3)$$

We calculated the Gibbs free energies for each of these reactions at the annealing temperature of 700 °C to determine the most viable reaction scheme. As SRO has not been synthesized before in a molten salt media, there are no thermodynamic data available for these conditions. Thus, we considered the case in the absence of the salt flux as an approximation for the reaction conditions employed herein.[89,90] On the basis of our calculations, we determined that reactions 1 and 2 are both spontaneous and favorable, with $\Delta G° = -37.18$ and -24.15 kJ/mol, respectively, with reaction 1 being slightly more favorable.

However, if we consider the possibility of SrO, which is formed from the decomposition of $Sr(OH)_2 \cdot 8H_2O$ at 530 °C,[91] reacting with either CO_2 in air or decomposed surfactants to form $SrCO_3$, the side reaction 4 must be considered.

$$SrO + CO_{2(g)} \rightarrow SrCO_3 \quad (4)$$

Upon calculation of the Gibbs free energy of reaction 4, it is found to be significantly more favorable, with $\Delta G° = -67.03$ kJ/mol. These calculations suggest that once SrO forms from the decomposition of the hydroxide, it can react with any carbon dioxide present, thereby forming $SrCO_3$. Following its formation, the $SrCO_3$ becomes soluble in the molten salt, reacting with the RuO_2 nanoparticles to form $SrRuO_3$. Reaction 4 would also be consistent with our observations of a persistent $SrCO_3$ impurity present within many of the samples synthesized using surfactants.

To confirm this, we investigated the reaction pathway via a temperature-dependent XRD analysis to determine what species were being dissolved into the molten flux. At low temperatures, the diffraction pattern is dominated by NaCl, KCl, and the Pt sample holder (Supporting Information, Figure S4), the former being expected, given the large amount of salt in the reaction mixture. A small amount of RuO_2 can be observed, although it is difficult to identify the Sr-containing phase, probably because of its low concentration and peak overlap. Upon heating, we observe the formation of two peaks around 25° in 2θ (shown in Figure 5), corresponding to the most intense peaks, namely, 111 and 021, of $Sr(CO)_3$ and these represent the most intense peaks in the XRD pattern of the compound (JCPDS# 00-005-0418). These peaks grow as the surfactant is decomposed, which is consistent with the TGA/DTA results (Figure 3), obtained from ~200 to 400 °C; peak intensities remain constant above 450 °C.

Because we have not observed any significant amount of SrO by any experimental technique, these results suggest that rather than forming $SrCO_3$ from SrO directly, $SrCO_3$ is likely generated from the partially hydrated strontium hydroxide[91] precursor during surfactant decomposition, as shown below in reaction 5.

$$Sr(OH)_2 \cdot xH_2O + CO_2 \rightarrow SrCO_3 + (x+1)H_2O \quad (5)$$

Calculation of the Gibbs free energy for reaction 5 at a reasonable temperature of 200 °C has rendered a very favorable value of $\Delta G° = -87.96$ kJ/mol. Hence, from the above analysis, we can conclude that the possible reaction mechanism is as follows: first $SrCO_3$ is formed from the direct reaction of strontium hydroxide with CO_2 (reaction 5), which subsequently reacts with the RuO_2 nanoparticles in the melt (reaction 2) to form SRO. Consistent with our investigation of the shape controlling effects associated with the surfactant molecules, the XRD data suggest that the surfactant also contributes to the conversion of strontium hydroxide to $SrCO_3$, providing insight into an additional role of the surfactant for this particular molten salt synthesis reaction.

3.6. Optimized SRO Product. Upon optimization of individual reaction conditions, we aimed to combine these optimized parameters within one reaction with the intent of creating the "best" strontium ruthenate sample, which we herein define as consisting of a reasonably monodisperse distribution of the smallest, most highly faceted SRO particles (sample TT). SEM analysis of the product showed that the SRO particles consisted of mainly octahedra (Figure 6A, B), including some structures which appeared to be truncated and incomplete. As compared with a previous sample prepared with 1% mineral oil in Triton X-100, the sizes of as-generated SRO particles are smaller, measuring 126 ± 45 nm. These data demonstrate that these conditions are in fact optimized for the synthesis of a predominantly octahedral morphology of SRO particles.

The XRD data (Figure 6C) confirms that the particles are $SrRuO_3$ with minute RuO_2 impurity peaks present. The HRTEM image (Figure 6D) obtained from an individual SRO octahedron reveals the single-crystalline nature of our particles. Moreover, neither apparent defects nor dislocations of the structure were observed. Furthermore, the spacings between the observed

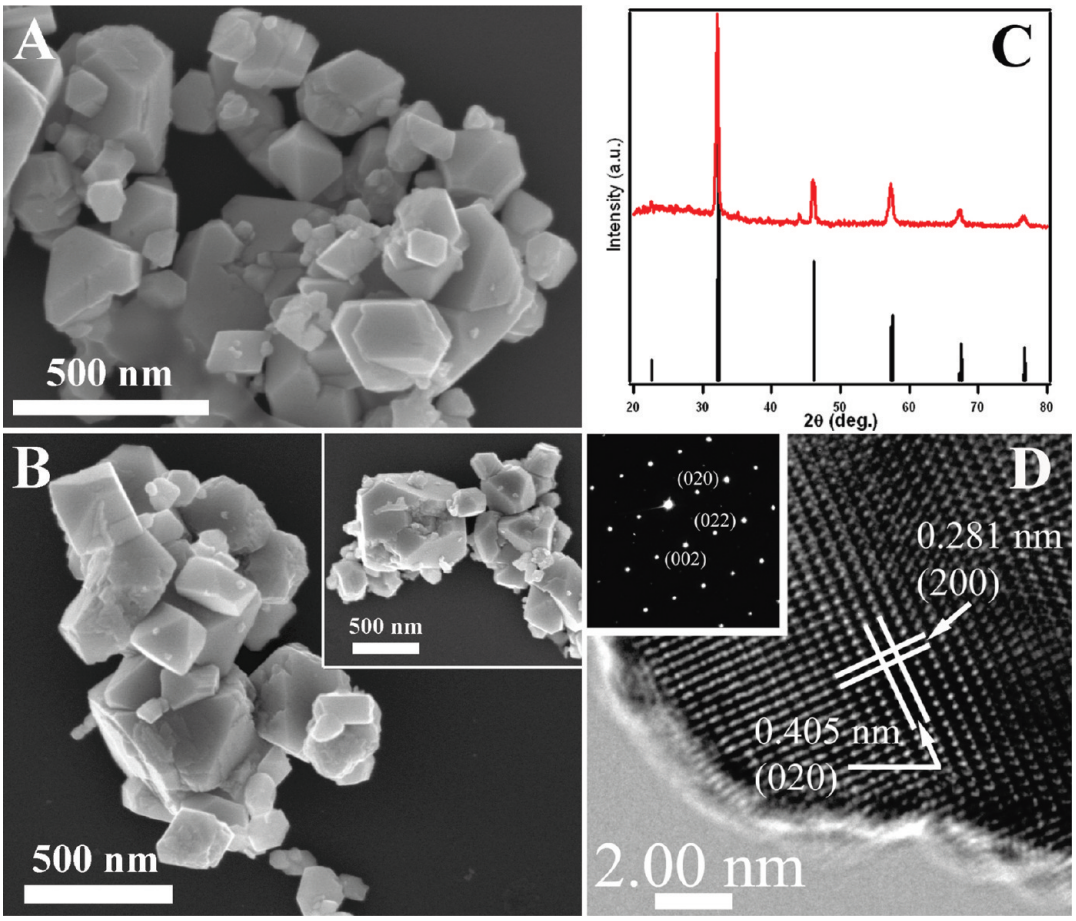

Figure 6. SEM images (A and B) and corresponding XRD data (C) of our as-prepared sample (red) by comparison with the JCPDS standard (#82-2156) for pure $SrRuO_3$ (black). HRTEM and SAED (inset) data (D) for a $SrRuO_3$ sample prepared under optimized reaction conditions.

lattice fringes were measured to be 0.281 and 0.405 nm, which are in good agreement with the (200) and (020) planes of orthorhombic SRO, respectively. Moreover, these results are consistent with the corresponding SAED pattern (Figure 6D inset). In addition, the sharpness of the spots observed in the diffraction pattern provides further evidence for the intrinsic single-crystalline nature of our as-synthesized SRO particles.

3.7. Property Characterization. Next, we aimed to investigate the properties intrinsic to the submicrometer SRO particles, in particular, their magnetic, electronic, and electrochemical attributes. Figure 7A represents the field-dependence of the magnetization at 2, 150, and 300 K. The $M-H$ curves at 2 and 150 K show moderate coercive fields, which are absent at 300 K, which is above the Curie temperature, T_C, of bulk SRO. The temperature dependence of the magnetization, M, of the SRO particles is plotted in Figure 7B after cooling in zero-field (ZFC) and cooling in a field of 500 Oe (FC). The FC and ZFC curves separate below ~170 K, below which the FC curve increases monotonically, like a ferromagnetic order parameter, and the ZFC data show a distinct peak at ~150 K. Field−temperature hysteresis of this sort is a signature of ferromagnets with domains, and so we conclude that ferromagnetic order occurs near 170 K. This is reasonably close to the 160 K Curie temperature of bulk SRO,[8,20,31] as might be expected given the large size of the particles (126 ± 45 nm). The second peak in the ZFC $M(T)$ at 147 K may indicate an additional modification to the magnetic structure, such as either a canted spin or helical structure, that can be saturated or otherwise suppressed in a 500 Oe field.

More importantly, the magnetic data confirms that as-synthesized particles are primarily composed of $SrRuO_3$ rather than the other well-known strontium ruthenate phases, that is, $Sr_3Ru_2O_7$ and $Sr_4Ru_3O_{10}$. These two strontium ruthenate phases exhibit ferromagnetic behavior analogous to $SrRuO_3$, albeit with very different Curie temperatures. In $Sr_3Ru_2O_7$, for example, the transition to the paramagnetic phase occurs at T_c = 105 K, whereas for $Sr_4Ru_3O_{10}$, the shift occurs at T_c = 148 K.[92] It is possible that the secondary peak in the ZFC $M(T)$ at 147 K corresponds to the presence of a small amount of $Sr_4Ru_3O_{10}$, at levels that are not detected in our X-ray diffraction experiments. While the presence of Sr_2RuO_4 could be detected by the observation of a partial Meissner signal at its superconducting transition temperature of 1.5 K,[28] our measurements only extend to 2 K, so we cannot comment on this possibility. Altogether, by combining the magnetization data with our XRD, HRTEM, and SAED analyses, we conclude that our particles are overwhelmingly $SrRuO_3$, although we cannot rule out the possibility that small amounts of $Sr_4Ru_3O_{10}$ and Sr_2RuO_4 may also be present.

Subsequent to magnetic analysis, we investigated the transport properties of our as-synthesized particles. First, we analyzed a control film, composed of SRO particles which had not been sintered. This film evinced a very low, noisy, and nonlinear response, most likely because of poor conductivity throughout

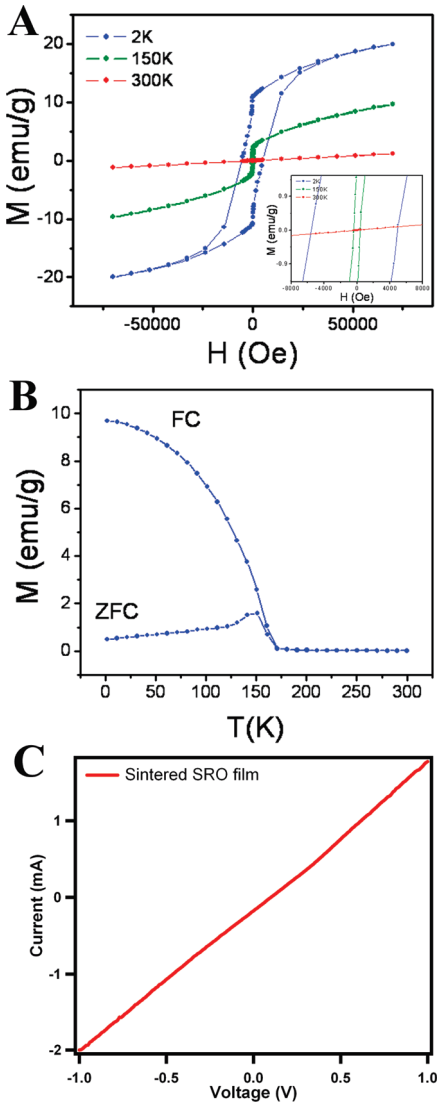

Figure 7. Field-dependence of magnetization at 2, 150, and 300 K, respectively, (A) as well as the temperature dependence of the magnetization (B) measured for SRO particles and a typical $I-V$ curve of a sintered film of SRO particles, demonstrating excellent conductivity (C).

the sample. As such, these data are not presented herein. Conversely, investigation of the sintered SRO film consisting of constituent octahedra-shaped particles revealed a near linear current−voltage response (Figure 7C), as expected from the metallic behavior and highly conductive nature of SRO.[11,27,62] Analysis of the curve elucidates a resistivity of 53 Ω·cm, which is significantly higher than values previously reported, for example, on the order of 200 $\mu\Omega\cdot$cm.[11,27,62] The difference can be attributed to several contributing factors. First, previous reports measured the resistivity of SRO thin films, whereas we have been collecting conductivity measurements on a relatively porous film, formed by sintering our particles together. Therefore, the increase in resistivity, as compared with literature values, can be attributed to poor interconnectivity within the particle network. Second, the contact between the probes and the film may not have been ideal, thereby introducing a finite contact resistance between the film and the probe. As such, the combination of these two factors can conceivably account for the increased resistivity we have observed for our sintered SRO films.

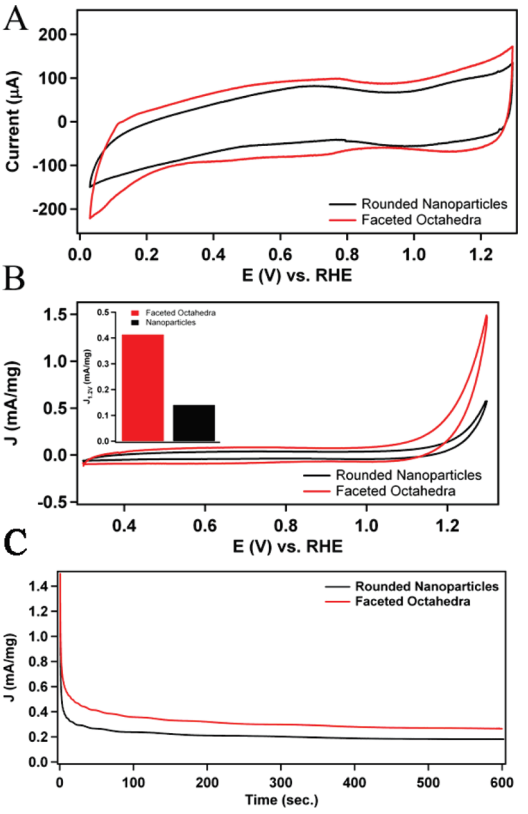

Figure 8. Cyclic voltammograms (A) obtained for as-synthesized $SrRuO_3$ rounded particles and faceted octahedra in a 0.1 M $HClO_4$ solution at 10 mV/s. Voltammetry curves (B) of a mass-normalized methanol oxidation process involving $SrRuO_3$ particles and faceted octahedra in a 0.5 M methanol/0.1 M $HClO_4$ solution at 10 mV/s. The mass-specific methanol oxidation activity of the $SrRuO_3$ particles is shown at 1.2 V. Time dependence of a mass-specific methanol oxidation activity (C) of $SrRuO_3$ nanostructures after a potential step from 0 to 1.25 V in a 0.5 M methanol/0.1 M $HClO_4$ solution at room temperature.

3.8. MOR Activity of SRO Nanoparticles. The structure-dependent MOR activity of $SrRuO_3$ was studied by comparing the activity of well-defined faceted octahedra with rounded nanoparticles, all possessing similar sizes. Initially, stationary electrode cyclic voltammograms (CVs) of as-prepared samples were obtained with glassy carbon electrodes (GCEs) loaded with $SrRuO_3$ nanoparticles (Figure 8A). The CVs are featureless over the relevant potential region, strongly indicating that the nanoparticles are sufficiently stable and do not undergo unwanted electrochemical processes. These nanostructured electrodes maintain a significantly enhanced response as compared with a bare GCE (Supporting Information, Figure S5A), confirming that the nanostructures are electrochemically active and maintain electrical contact with the GCE substrate.

The MOR activity of $SrRuO_3$ nanostructures was determined by CV (Figure 8B) in the presence of a 0.1 M $HClO_4$ solution containing 0.5 M methanol. The measured currents in this case have been normalized to the mass of catalyst loaded onto the GCE so as to provide insight into the mass activity of these nanostructures. The CV curves reveal that the faceted octahedra maintain significantly enhanced MOR activity as evidenced by the increased anodic current above 1.0 V. In fact, the mass-specific methanol oxidation activity measured at 1.2 V (inset of Figure 8B) for the faceted nanoparticles is nearly four times

dx.doi.org/10.1021/cm1029497 |*Chem. Mater.* 2011, 23, 3277–3288

greater than that of the rounded nanoparticles. The fairly linear increase in the oxidation current has been previously observed in the literature as it is thought to arise from an increase in the number of surface oxide species at higher potential, which are more active toward methanol oxidation.[44] It is important to highlight that the bare GCE electrode essentially yielded no anodic response in the presence of methanol (Supporting Information, Figure S5B), thereby confirming that the electro-oxidation process is solely derived from the $SrRuO_3$ catalyst particles.

In addition, the CVs also reveal that the faceted octahedra maintain an onset potential for methanol oxidation at 0.9 V, which is approximately 100 mV lower than the measured onset potential of the rounded nanoparticles (1.0 V). A corresponding shift to lower potentials in the case of MOR indicates suppression of the anodic overpotential, thereby suggesting enhanced anodic activities in the case of well-defined faceted octahedra. Although these metal oxide catalysts are not as active as traditional platinum and platinum alloy catalysts, they maintain comparable activities to other perovskite-based catalysts previously presented in the literature.[43−45] The low activity of these metal oxide-based catalysts is thought to arise from the slow kinetics of the initial oxidative dehydration of the adsorbed methanol.[44]

To further study the activity and stability of the $SrRuO_3$, chronoamperometry (CA) was performed in a 0.5 M $HClO_4$ electrolyte containing 0.5 M methanol (Figure 8C) so as to determine the methanol tolerance of as-prepared nanostructures. After stepping the potential from 0 to 1.25 V, the current rapidly decays toward a steady value. Based upon the CA data, both the octahedral and the rounded particles maintain similar rates of current decay and both achieve a steady state current density that is approximately 1% of the initial current density after 500 s, suggesting that they possess similar methanol tolerance. However, the CA data again highlight the enhanced activity of the faceted octahedral particles, as the steady current density of this sample was found to be 0.26 mA/mg after 600 s, which is nearly 1.5 fold times higher than that of the rounded nanoparticles (0.18 mA/mg) after an identical operating time.

To gain further insight into the origin of the enhancement in mass activity in the faceted octahedra, complementary BET analysis of the surface area revealed that the faceted particles possess a large surface area, specifically 11.427 m^2/g, which is four times the surface area of their rounded counterparts, which maintained a surface area of 2.856 m^2/g. The observed methanol oxidation current densities at 1.2 V were normalized to the measured geometric surface area of the catalyst so as to determine the intrinsic surface area activity of the SRO nanoparticles and octahedra. On the basis of this protocol, the calculated surface area activities for both rounded and faceted particles were determined to be nearly identical at 4.9 and 3.7 $\mu A/cm^2$, respectively. Based upon the measured specific activities, it is evident that the rounded and octahedral SRO particles maintain identical active sites for the oxidation of methanol. Since methanol electro-oxidation at the metal oxide is entirely a surface mediated process,[40,41,93,94] the enhanced mass activity in the octahedral particles is likely derived from their inherently larger surface area, which translates to a proportionally larger number of active surface sites per unit of mass as compared with their rounded nanoparticle counterparts.

4. CONCLUSIONS

By employing the simple molten salt method, we have successfully demonstrated the synthesis of single-crystalline $SrRuO_3$ submicrometer-sized particles. Moreover, through a systematic study of the experimental parameters of this synthetic protocol, namely, salt, annealing time, annealing temperature, cooling rate, nature of precursors, gaseous atmosphere, and surfactant, we have been able to correlate the individual effects of these variables upon the resulting chemical composition, size, and morphology of as-generated $SrRuO_3$ particles. These data have allowed for reasonably reliable and predictive control over the final product.

Based upon these systematic protocols coupled with the synthesis of a correspondingly large number of samples, we have deduced that the NaCl/KCl eutectic at an annealing temperature of 700 °C was optimal for reliably producing not only the correct chemical composition but also the most uniform morphology. Moreover, minimization of reaction times to periods of 0 to 2 h was crucial in terms of maintaining an overall smaller particle size, whereas inclusion of a relatively fast cooling rate (e.g., ∼100 °C/min) quenched the reaction, resulting in the formation of smaller, rounded SRO particles, measuring 149 ± 100 nm. Moreover, altering the gas flow through the furnace clearly demonstrated the necessity of an air atmosphere for producing SRO under these experimental conditions. Based upon all of our data, we found that the most important reaction parameter for morphology control was the choice of surfactant. Specifically, the addition of a 1% mixture of mineral oil in Triton X-100 surfactant yielded highly faceted SRO octahedra, measuring 126 ± 45 nm in size.

We have demonstrated that the inclusion of the surfactant is necessary to fulfill numerous roles under molten salt conditions. First, we have shown that the surfactant can affect the final morphology by controlling the corresponding shape and size of the reaction intermediates. Second, the presence of surfactant yields significantly decreased aggregation of the resultant particles. Lastly, decomposition of the surfactant results in the conversion of strontium hydroxide to strontium carbonate, as evinced by our *in situ* temperature-dependent XRD measurements. This result points to the reaction pathway as occurring via conversion of the strontium hydroxide precursor to $SrCO_3$, which subsequently reacts with the RuO_2 nanoparticles to form $SrRuO_3$.

Subsequent characterization of our as-synthesized SRO particles by magnetic, transport, and spectroscopic techniques has revealed properties, corresponding to bulk SRO: ferromagnetism with T_c ∼ 155 K; high conductivity as a sintered film; and the presence of IR peaks consistent with reported transitions with the possibility of a small amount of carbonate impurities. Most significant was the investigation of our as-synthesized SRO particles as MOR catalysts for direct methanol fuel cells. Our particles were in fact MOR active. Specifically, while we observed comparable surface area activities, our well-defined faceted octahedra exhibited a 4-fold increase in electrochemical mass-activity as compared with analogous smooth, rounded particles, demonstrating a clear advantage of faceted particles from the point of view of applications.

■ ASSOCIATED CONTENT

Supporting Information. Details about Materials and Methods as well as an exploration of specific synthetic parameters including annealing temperatures, the nature of precursors, cooling rates, the ratio of reagents, and postprocessing protocols, are thoroughly discussed and corroborated by additional SEM and XRD data. Spectroscopy and electrochemistry results are also provided. This material is available free of charge via the Internet at http://pubs.acs.org.

AUTHOR INFORMATION

Corresponding Author

*Phone: 631-632-1703 or 631-344-3178. E-mail: sswong@notes.cc.sunysb.edu or sswong@bnl.gov.

ACKNOWLEDGMENT

Research (including support for MCA and SSW as well as for the magnetic and electrochemical experiments) was supported by the U.S. Department of Energy, Basic Energy Sciences, Materials Sciences and Engineering Division. R.H. and J.B.P. acknowledge financial support provided by the National Science Foundation (NSF) through Collaborative Research in Chemistry (CRC), Grant CHE0714183. We acknowledge that this work was done in part at the Center for Functional Nanomaterials (CFN) at Brookhaven National Laboratory (BNL).We also acknowledge Radoslav R. Adzic for providing the instruments and supplies for the electrochemical testing and Meng Li for her assistance with conducting the electrochemical experiments. The Rigaku diffractometer was supported by NASA Grant MFRP07-0022 (J.B.P.). We also thank James Quinn, Susan van Horn, and Eli Sutter for their assistance with electron microscopy as well as Carlos Marques for his help with the differential thermal analysis measurements. We also thank Martin Schoonen for assistance with the BET analysis.

REFERENCES

(1) Callaghan, A.; Moeller, C. W.; Ward, R. *Inorg. Chem.* **2002**, *5*, 1572.
(2) Noro, Y.; Miyahara, S. *J. Phys. Soc. Jpn.* **1969**, *27*, 518.
(3) Bouchard, R. J.; Gillson, J. L. *Mater. Res. Bull.* **1972**, *7*, 873.
(4) Fukunaga, F.; Tsuda, N. *J. Phys. Soc. Jpn.* **1994**, *63*, 3798.
(5) Kanbayasi, A. *J. Phys. Soc. Jpn.* **1976**, *41*, 1876.
(6) Lee, H. N.; Christen, H. M.; Chisholm, M. F.; Rouleau, C. M.; Lowndes, D. H. *Appl. Phys. Lett.* **2004**, *84*, 4107.
(7) Bensch, W.; Schmalle, H. W.; Reller, A. *Solid State Ion.* **1990**, *43*, 171.
(8) Rondinelli, J. M.; Caffrey, N. M.; Sanvito, S.; Spaldin, N. A. *Phys. Rev. B* **2008**, *78*, 155107.
(9) Toyota, D.; Ohkubo, I.; Kumigashira, H.; Oshima, M.; Ohnishi, T.; Lippmaa, M.; Takizawa, M.; Fujimori, A.; Ono, K.; Kawasaki, M.; Koinuma, H. *Appl. Phys. Lett.* **2005**, *87*, 162508.
(10) Gausepohl, S. C.; Lee, M.; Char, K.; Rao, R. A.; Eom, C. B. *Phys. Rev. B* **1995**, *52*, 3459.
(11) Allen, P. B.; Berger, H.; Chauvet, O.; Forro, L.; Jarlborg, T.; Junod, A.; Revaz, B.; Santi, G. *Phys. Rev. B* **1996**, *53*, 4393.
(12) Gausepohl, S. C.; Lee, M.; Rao, R. A.; Eom, C. B. *Phys. Rev. B* **1996**, *54*, 8996.
(13) Jeng, H.-T.; Lin, S.-H.; Hsue, C.-S. *Phys. Rev. Lett.* **2006**, *97*, 067002.
(14) Maiti, K. *Phys. Rev. B* **2006**, *73*, 235110.
(15) Mazin, I. I.; Singh, D. J. *Phys. Rev. B* **1997**, *56*, 2556.
(16) Santi, G.; Jarlborg, T. *J. Phys.: Condens. Matter* **1997**, *9*, 9563.
(17) Singh, D. J. *J. Appl. Phys.* **1996**, *79*, 4818.
(18) Kostic, P.; Okada, Y.; Collins, N. C.; Schlesinger, Z.; Reiner, J. W.; Klein, L.; Kapitulnik, A.; Geballe, T. H.; Beasley, M. R. *Phys. Rev. Lett.* **1998**, *81*, 2498.
(19) Ahn, J. S.; Bak, J.; Choi, H. S.; Noh, T. W.; Han, J. E.; Bang, Y.; Cho, J. H.; Jia, Q. X. *Phys. Rev. Lett.* **1999**, *82*, 5321.
(20) Fujioka, K.; Okamoto, J.; Mizokawa, T.; Fujimori, A.; Hase, I.; Abbate, M.; Lin, H. J.; Chen, C. T.; Takeda, Y.; Takano, M. *Phys. Rev. B* **1997**, *56*, 6380.
(21) Kim, H.-D.; Noh, H.-J.; Kim, K. H.; Oh, S. J. *Phys. Rev. Lett.* **2004**, *93*, 126404.
(22) Kim, J.; Chung, J.; Oh, S. J. *Phys. Rev. B* **2005**, *71*, 121406.
(23) Okamoto, J.; Mizokawa, T.; Fujimori, A.; Hase, I.; Nohara, M.; Takagi, H.; Takeda, Y.; Takano, M. *Phys. Rev. B* **1999**, *60*, 2281.
(24) Park, J.; Oh, S.-J.; Park, J. H.; Kim, D. M.; Eom, C. B. *Phys. Rev. B* **2004**, *69*, 085108.
(25) Siemons, W.; Koster, G.; Vailionis, A.; Yamamoto, H.; Blank, D. H. A.; Beasley, M. R. *Phys. Rev. B* **2007**, *76*, 075126.
(26) Takizawa, M.; Toyota, D.; Wadati, H.; Chikamatsu, A.; Kumigashira, H.; Fujimori, A.; Oshima, M.; Fang, Z.; Lippmaa, M.; Kawasaki, M.; Koinuma, H. *Phys. Rev. B* **2005**, *72*, 060404.
(27) Cao, G.; McCall, S.; Shepard, M.; Crow, J. E.; Guertin, R. P. *Phys. Rev. B* **1997**, *56*, 321.
(28) Cao, G.; Alexander, C. S.; McCall, S.; Crow, J. E.; Guertin, R. P. *Mater. Sci. Eng., B* **1999**, *63*, 76.
(29) Kobayashi, H.; Nagata, M.; Kanno, R.; Kawamoto, Y. *Mater. Res. Bull.* **1994**, *29*, 1271.
(30) Antognazza, L.; Char, K.; Geballe, T. H.; King, L. L. H.; Sleight, A. W. *Appl. Phys. Lett.* **1993**, *63*, 1005.
(31) Gausepohl, S. C.; Lee, M.; Antognazza, L.; Char, K. *Appl. Phys. Lett.* **1995**, *67*, 1313.
(32) Miéville, L.; Koller, E.; Triscone, J. M.; Decroux, M.; Fischer, O.; Williams, E. J. *Phys. Rev. B* **1996**, *54*, 9525.
(33) Wu, X. D.; Foltyn, S. R.; Dye, R. C.; Coulter, Y.; Muenchausen, R. E. *Appl. Phys. Lett.* **1993**, *62*, 2434.
(34) Ahn, C. H.; Hammond, R. H.; Geballe, T. H.; Beasley, M. R.; Triscone, J. M.; Decroux, M.; Fischer, O.; Antognazza, L.; Char, K. *Appl. Phys. Lett.* **1997**, *70*, 206.
(35) Prins, M. W. J.; Grosse-Holz, K. O.; Muller, G.; Cillessen, J. F. M.; Giesbers, J. B.; Weening, R. P.; Wolf, R. M. *Appl. Phys. Lett.* **1996**, *68*, 3650.
(36) Harnagea, C.; Cojocaru, C. V.; Nechache, R.; Gautreau, O.; Rosei, F.; Pignolet, A. *Int. J. Nanotechnol.* **2008**, *5*, 930.
(37) Cross, J. S.; Fujiki, M.; Tsukada, M.; Matsuura, K.; Otani, S.; Tomotani, M.; Kataoka, Y.; Kotaka, Y.; Goto, Y. *Integr. Ferroelectr.* **1999**, *25*, 265.
(38) Kodaira, T.; Nishio, K.; Yamaguchi, I.; Suzuki, S.; Tsukada, K.; Tsuchiya, T. *J. Sol-Gel Sci. Technol.* **2003**, *26*, 1049.
(39) Scott, J. F.; Araujo, C. A. P. D. *Science* **1989**, *246*, 1400.
(40) Lan, A.; Mukasyan, A. S. *J. Phys. Chem. C* **2007**, *111*, 9573.
(41) White, J. H.; Sammells, A. F. *J. Electrochem. Soc.* **1993**, *140*, 2167.
(42) Serov, A.; Kwak, C. *Appl. Catal., B* **2009**, *90*, 313.
(43) Yu, H.-C.; Fung, K.-Z.; Guo, T.-C.; Chang, W.-L. *Electrochim. Acta* **2004**, *50*, 811.
(44) White, J. H.; Sammells, A. F. *J. Electrochem. Soc.* **1993**, *140*, 2167.
(45) Yue, Z.; Zhanhui, Y.; Hengbin, Z.; Xuejing, C.; Se, L.; Shujia, L.; Chiachung, S. *Mater. Chem. Phys.* **1999**, *57*, 285.
(46) Deshpande, K.; Mukasyan, A. S.; Varma, A. *J. Power Sources* **2006**, *158*, 60.
(47) Lan, A.; Mukasyan, A. S. *J. Phys. Chem. C* **2007**, *111*, 9573.
(48) Mao, Y.; Banerjee, S.; Wong, S. S. *J. Am. Chem. Soc.* **2003**, *125*, 15718.
(49) Mao, Y.; Wong, S. S. *Adv. Mater.* **2005**, *17*, 2194.
(50) Mao, Y. B.; Banerjee, S.; Wong, S. S. *Chem. Commun.* **2003**, 408.
(51) Park, T.-J.; Mao, Y.; Wong, S. S. *Chem. Commun.* **2004**, 2708.
(52) Zhou, H.; Mao, Y.; Wong, S. S. *Chem. Mater.* **2007**, *19*, 5238.
(53) Banerjee, S.; Kim, D. I.; Robinson, R. D.; Herman, I. P.; Mao, Y. B.; Wong, S. S. *Appl. Phys. Lett.* **2006**, *89*, 223130.
(54) Park, T.-J.; Papaefthymiou, G. C.; Viescas, A. J.; Moodenbaugh, A. R.; Wong, S. S. *Nano Lett.* **2007**, *7*, 766.
(55) Zhou, H.; Mao, Y.; Wong, S. S. *J. Mater. Chem.* **2007**, *17*, 1707.
(56) Eom, C. B.; Cava, R. J.; Fleming, R. M.; Phillips, J. M.; Van Dover, R. B.; Marshall, J. H.; Hsu, J. W. P.; Krajewski, J. J.; Peck, J.; W., F. *Science* **1992**, *258*, 1766.
(57) Eom, C. B.; Van Dover, R. B.; Phillips, J. M.; Werder, D. J.; Marshall, J. H.; Chen, C. H.; Cava, R. J.; Fleming, R. M.; Fork, D. K. *Appl. Phys. Lett.* **1993**, *63*, 2570.
(58) Vasco, E.; Dittmann, R.; Karthauser, S.; Waser, R. *Appl. Phys. Lett.* **2003**, *82*, 2497.
(59) Xia, J.; Siemons, W.; Koster, G.; Beasley, M. R.; Kapitulnik, A. *Phys. Rev. B* **2009**, *79*, 140407.

(60) Hong, W.; Lee, H. N.; Yoon, M.; Christen, H. M.; Lowndes, D. H.; Suo, Z.; Zhang, Z. *Phys. Rev. Lett.* **2005**, *95*, 095501.
(61) Vasco, E.; Dittmann, R.; Karthäuser, S.; Waser, R. *Appl. Phys. A: Mater. Sci. Process.* **2004**, *79*, 1461.
(62) Pagnaer, J.; Nelis, D.; Mondelaers, D.; Vanhoyland, G.; D'Haen, J.; Van Bael, M. K.; Van den Rul, H.; Mullens, J.; Van Poucke, L. C. *J. Eur. Ceram. Soc.* **2004**, *24*, 919.
(63) Mercurio, J. P.; Yi, J. H.; Manier, M.; Thomas, P. *J. Alloys Compd.* **2000**, *308*, 77.
(64) Galal, A.; Darwish, S. A.; Atta, N. F.; Ali, S. M.; Abd El Fatah, A. A. *Appl. Catal., A* **2010**, *378*, 151.
(65) Walker, J.; King, R. B.; Tannenbaum, R. *J. Solid State Chem.* **2007**, *180*, 2290.
(66) Filankembo, A.; Giorgio, S.; Lisiecki, I.; Pileni, M. P. *J. Phys. Chem. B* **2003**, *107*, 7492.
(67) Yoon, K. H.; Cho, Y. S.; Kang, D. H. *J. Mater. Sci.* **1998**, *33*, 2977.
(68) Mao, Y. B.; Park, T.-J.; Zhang, F.; Zhou, H.; Wong, S. S. *Small* **2007**, *3*, 1122.
(69) Song, X. C.; Yang, E.; Ma, R.; Chen, H. F.; Zhao, Y. *J. Nanopart. Res.* **2008**, *10*, 709.
(70) Sui, Y.; Fu, W.; Yang, H.; Zeng, Y.; Zhang, Y.; Zhao, Q.; Li, Y.; Zhou, X.; Leng, Y.; Li, M.; Zou, G. *Cryst. Growth Des.* **2010**, *10*, 99.
(71) Quan, Z.; Li, C.; Zhang, X.; Yang, J.; Yang, P.; Zhang, C.; Lin, J. *Cryst. Growth Des.* **2008**, *8*, 2384.
(72) Li, C.; Cai, W.; Cao, B.; Sun, F.; Li, Y.; Kan, C.; Zhang, L. *Adv. Funct. Mater.* **2006**, *16*, 83.
(73) Xiong, Y.; Xia, Y. *Adv. Mater.* **2007**, *19*, 3385.
(74) Sun, H.-T.; Fujii, M.; Nitta, N.; Shimaoka, F.; Mizuhata, M.; Yasuda, H.; Deki, S.; Hayashi, S. *J. Am. Ceram. Soc.* **2008**, *91*, 4158.
(75) Wang, W.; Xu, C.; Wang, G.; Liu, Y.; Zheng, C. *Adv. Mater.* **2002**, *14*, 837.
(76) Wu, X.; Liang, Y.; Liu, R.; Li, Y. *Mater. Res. Bull.* **2010**, *45*, 594.
(77) Wang, W.; Zhang, G. *J. Cryst. Growth* **2009**, *311*, 4275.
(78) Wang, D.; Chu, X.; Gong, M. *Sens. Actuators, B* **2006**, *117*, 183.
(79) Mitsuda, K.; Kimura, H.; Murahashi, T. *J. Mater. Sci.* **1989**, *24*, 413.
(80) Liu, Y.; Yang, W.; Dai, Z.; Chen, H.; Yang, X.; Hou, D. *Mater. Chem. Phys.* **2008**, *112*, 381.
(81) Yaokawa, J.; Oikawa, K.; Anzai, K. *CALPHAD: Comput. Coupling Phase Diagrams Thermochem.* **2007**, *31*, 155.
(82) Mao, Y.; Wong, S. S. *J. Am. Chem. Soc.* **2006**, *128*, 8217.
(83) Cótica, L. F.; Moreto, J. A.; Szmoski, R. M.; Paesano, A., Jr; Santos, I. A. *J. Alloys Compd.* **2009**, *467*, 424.
(84) Du, N.; Xu, Y.; Zhang, H.; Zhai, C.; Yang, D. *Nanoscale Res. Lett.* **2010**, *5*, 1295.
(85) Kim, J. H.; Myung, S. T.; Sun, Y. K. *Electrochim. Acta* **2004**, *49*, 219.
(86) Rørvik, P. M.; Lyngdal, T.; Sæterli, R.; van Helvoort, A. T. J.; Holmestad, R.; Grande, T.; Einarsrud, M.-A. *Inorg. Chem.* **2008**, *47*, 3173.
(87) Hu, C.; Xi, Y.; Liu, H.; Wang, Z. L. *J. Mater. Chem.* **2009**, *19*, 858.
(88) Voorhees, P. W. *Annu. Rev. Mater. Sci.* **1992**, *22*, 197.
(89) Dean, J. A. *Lange's Handbook of Chemistry*, 14th ed.; McGraw-Hill: New York, 1992.
(90) Jacob, K. T.; Lwin, K. T.; Waseda, Y. *Mater. Sci. Eng., B* **2003**, *103*, 152.
(91) Dinescu, R.; Preda, M. *J. Therm. Anal.* **1973**, *5*, 465.
(92) Crawford, M. K.; Harlow, R. L.; Marshall, W.; Li, Z.; Cao, G.; Lindstrom, R. L.; Huang, Q.; Lynn, J. W. *Phys. Rev. B* **2002**, *65*, 214412.
(93) Petrovic, S.; Rakic, V.; Jovanovic, D. M.; Baricevic, A. T. *Appl. Catal., B* **2006**, *66*, 249.
(94) Peña, M. A.; Fierro, J. L. G. *Chem. Rev.* **2001**, *101*, 1981.